MATERIAL SCIENCE

WS$_2$ ribbon arrays with defined chirality and coherent polarity

Guodong Xue[1,2]†, Ziqi Zhou[1,3]†, Quanlin Guo[1,4]†, Yonggang Zuo[5]†, Wenya Wei[6], Jiashu Yang[7], Peng Yin[2], Shuai Zhang[8], Ding Zhong[2], Yilong You[1], Xin Sui[9], Chang Liu[9], Muhong Wu[9], Hao Hong[1], Zhu-Jun Wang[10], Peng Gao[9], Qunyang Li[8], Libo Zhang[5], Dapeng Yu[11], Feng Ding[7]*, Zhongming Wei[3]*, Can Liu[2]*, Kaihui Liu[1,9,12]*

One-dimensional transition metal dichalcogenides exhibiting an enhanced bulk photovoltaic effect have the potential to exceed the Shockley–Queisser limit efficiency in solar energy harvest within *p-n* junction architectures. However, the collective output of these prototype devices remains a challenge. We report on the synthesis of single-crystalline WS$_2$ ribbon arrays with defined chirality and coherent polarity through an atomic manufacturing strategy. The chirality of WS$_2$ ribbon was defined by substrate couplings into tunable armchair, zigzag, and chiral species, and the polarity direction was determined by the ribbon-precursor interfacial energy along a coherent direction. A single armchair ribbon showed strong bulk photovoltaic effect and the further integration of ~1000 aligned ribbons with coherent polarity enabled upscaling of the photocurrent.

The ongoing global transition toward sustainable energy practices amplifies the urgency for efficient and versatile photovoltaic techniques. The bulk photovoltaic effect (BPVE)—a second-order nonlinear phenomenon in noncentrosymmetric materials that allows for direct conversion of solar energy into electrical current—provides a promising solution (*1–5*). Complementary to traditional *p-n* junction photovoltaics, BPVE holds the potential to circumvent the Shockley–Queisser limitation that intrinsically exists in conventional solar cells (*6–8*). One-dimensional (1D) transition metal dichalcogenides (TMDs), distinguished by their low internal symmetric structure and robust absorption in the visible light spectrum, align well with the prerequisites for BPVE (*9–11*).

To further upscale the TMD-based BPVE current through the interconnection of large 1D structures, several concurrent criteria must be satisfied: (i) A robust and strong photocurrent must be generated in 1D individuals that have specially defined chirality. (ii) Different 1D structures should have coherent polarities to ensure a constructive BPVE current collection. (iii) Parallel-aligned 1D arrays are preferred to facilitate large-scale solar cell integration. In this regard, a unidirectionally aligned array with specific axial chirality and coherent polarity is the prerequisite for advancing TMD-based BPVE devices from individual prototype concepts to massive integration applications.

Recently, progress has been made in modulating the macroscopic configurations of 1D TMDs, such as their orientations (*12–15*) and aspect ratios (*16–22*). However, the control over microscopic arrangements such as axial chirality and polarity direction has blocked progress (*23*). This challenge is compounded by the lack of an effective mechanism for controlling these structural geometries at the atomic level. A useful reference comes from the success of the chirality-controlled growth of 1D carbon nanotubes and graphene ribbons (*24–28*). However, the noncentrosymmetric lattice of TMDs with two elements in the hexagonal lattice even complicates the case of their 1D counterparts, which tends to produce twinned structures with reversed polarity. A strategy that provides atomic precise lattice arrangement is therefore required to address these synthetic challenges.

We propose an atomic manufacturing strategy for the deterministic fabrication of WS$_2$ ribbon arrays with defined chirality and coherent polarity. Our approach leverages the couplings between the WS$_2$ lattice and sapphire substrate with aligned steps, which determine the epitaxy orientation of the WS$_2$ lattice and guide the ribbon axis and therefore defines the ribbon chirality. The ribbon-precursor interface thermodynamically drives the unipolarity-terminated growth. As a result, armchair, zigzag, and chiral (both left- and right-handed) ribbon arrays (see definition in fig. S1) with coherent polarity are selectively fabricated. Various ribbons grown by an atomic manufacturing mechanism enable the investigation of chirality-dependent BPVE responses and highlight the utilization of mono-chirality ribbon arrays with coherent polarity to generate a constructive BPVE photocurrent.

Preseeded growth of the WS$_2$ ribbon arrays

The growth of WS$_2$ ribbon arrays was initiated by preseeded templates. Na$_2$WO$_4$ particles were deposited onto an a-plane sapphire (a-Al$_2$O$_3$) substrate by evaporating a thin Na$_2$WO$_4$ film, which subsequently served as the seeds for the growth of WS$_2$ ribbons (Fig. 1A). Sulfur atoms were supplied through the decomposition of an upper positioned ZnS plate (*29*) and stimulated the growth of the WS$_2$ ribbon arrays along the [1$\bar{1}$00] direction of a-Al$_2$O$_3$ at an elevated temperature of 930°C (Fig. 1B; materials and methods in the supplementary materials, S1.3).

Uniform WS$_2$ ribbon arrays with a typical length of ~150 μm and width of ~300 nm were obtained after a growth duration of 1 hour (Fig. 1C). The presence of characteristic E$^1_{2g}$ and A$_{1g}$ Raman modes, along with the corresponding intensity mapping, demonstrates the formation of crystalline WS$_2$ lattice structures (Fig. 1D and fig. S2). Some particles were occasionally observed at the terminal of the ribbons. Both S and W elements were uniformly distributed at the particles and the ribbons, confirming the seed-driven vapor-liquid-solid (VLS) growth mechanism of the WS$_2$ arrays (Fig. 1E).

With VLS growth, the morphology of the ribbons could be determined by the size of the preseeded particle templates and further manipulated by modulating the concentration of the Na$_2$WO$_4$ solution (*c*) during the film deposition (fig. S3). Specifically, both the average length and width increased in proportion to the size of the particles, with typical lengths of 38, 74, and 285 μm and widths of 110, 235, and 501 nm, respectively, when *c* was adjusted from 1, 10 to 30 mg mL^{-1} (a higher concentration of Na$_2$WO$_4$ led to larger particle sizes) (Fig. 1, F and G). Ribbons with widths under 100 nm and lengths extending to the millimeter scale can be successfully obtained at optimized growth conditions (fig. S4 and S5).

Confirmation of the coherent polarity direction

The WS$_2$ ribbons display coherent polarity along the entire array. As shown in Fig. 2A, high-angle annular dark-field scanning transmission
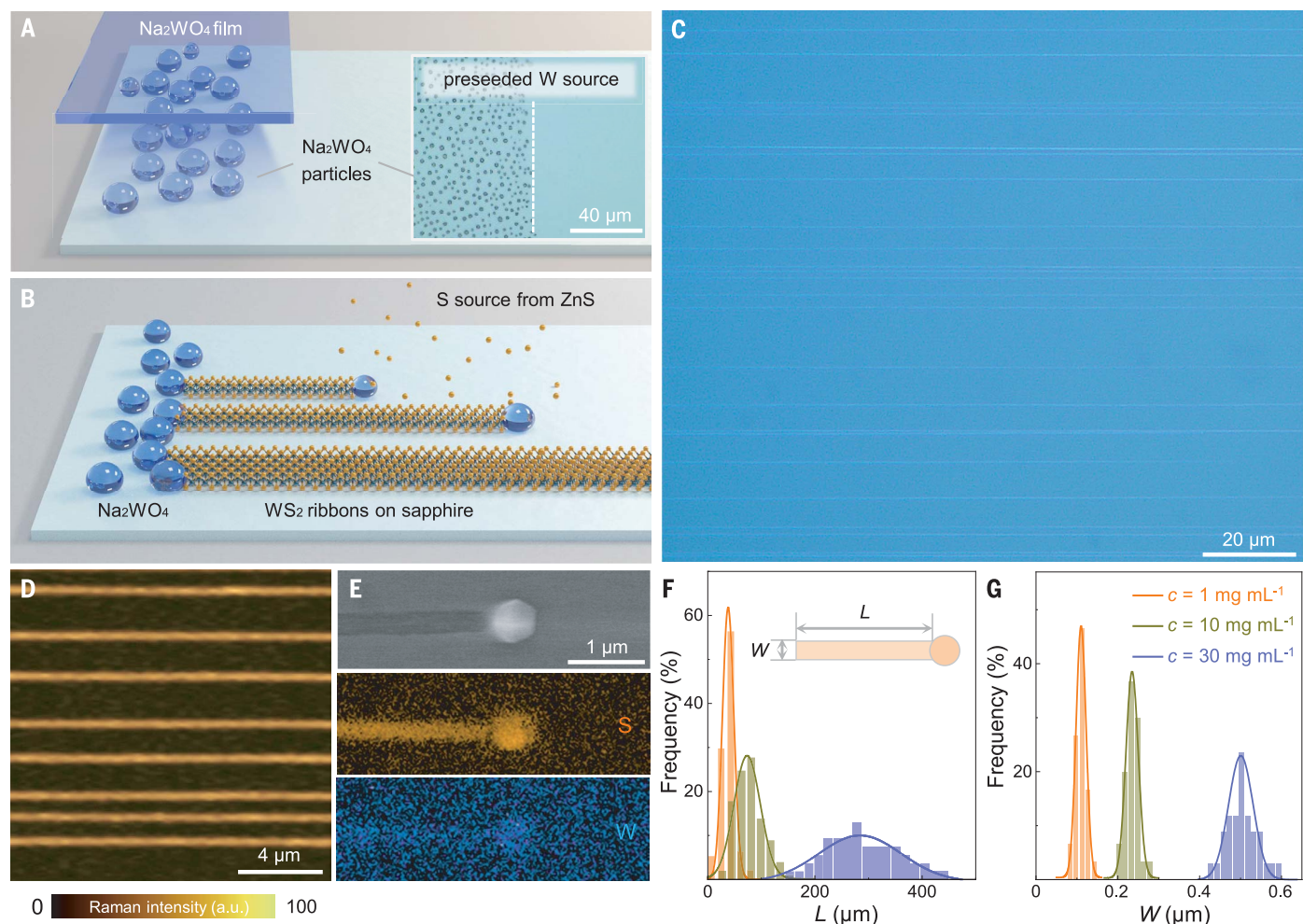
Fig. 1. Fabrication of the aligned WS₂ ribbon arrays. (**A**) Schematic of the preseeding of Na_2WO_4 particles on sapphire substrate. Insert shows typical optical image of the uniformly preseeded Na_2WO_4 templates. (**B**) Schematic for the VLS growth of WS₂ ribbons on sapphire substrate. (**C**) Optical image of the as-grown unidirectional WS₂ ribbon array. (**D**) Raman mapping of the ribbons based on the intensity of the E^1_{2g} vibration mode. (**E**) Scanning electron microscopy (SEM) image of the terminal region of a representative ribbon (upper panel) and the corresponding auger electron spectroscopy elemental mapping (middle panel, sulfur; lower panel, tungsten). (**F** and **G**) Statistical length and width distributions of the ribbons with predeposited Na_2WO_4 concentrations (*c*) of 1 mg mL^{-1}, 10 mg mL^{-1}, and 30 mg mL^{-1}. The insert in (F) indicates the definition of the width (W) and length (L) of a ribbon.

electron microscopy (HAADF-STEM) image shows the perfect hexagonal honeycomb lattice of the WS₂ ribbon and demonstrates that its zigzag edges were parallel to its axis (denoted as ZZ-Rs). The corresponding selected area electron diffraction (SAED) pattern contains two sets of conjugated Bragg peaks arising from the broken in-plane inversion symmetry of the WS₂ lattice (Fig. 2B), in which the first-order diffraction spots toward the W-sublattice possess an ~30% greater intensity than those of the S-sublattice. This intensity asymmetry is effective in identifying the polarity direction of WS₂ crystals (*30*). As shown in Fig. 2C, when an aperture was placed at the W-sublattice (purple circle in Fig. 2B), two adjacent ribbons preserved the consistent contrast in both the bright-field image (top panel) and the dark-field image (bottom panel), revealing their co-

herent polarity orientations. In addition, the atomic-resolution STEM images of the two ribbons further confirm their identical orientation at the atomic level (Fig. 2D).

To systematically examine the polarity coherence of many different ribbons, assembled arrays were studied through high-throughput nonlinear optical spectroscopy of second harmonic generation (SHG). We developed a method for simultaneously mapping the polarity directions of the separated ribbons. As illustrated in Fig. 2E, by covering a triangular single-crystal WS₂ monolayer domain on the top surfaces of ribbon arrays (ensuring the zigzag edges of WS₂ domain and ribbons are parallelly aligned), 0°-stacked overlapping regions naturally formed in the polarity coherent array case (Fig. 2E, top panel), leading to a consistent enhancement of the SHG signal. By

contrast, for the polarity incoherent array case (Fig. 2E, bottom panel), constructive and destructive SHG responses coexisted, corresponding to the noncentrosymmetric 0°-stacked regions and the centrosymmetric 180°-stacked regions, respectively. Experimentally, we observed a fourfold increase in the SHG intensity in the overlapping regions compared with that in bare ribbons, demonstrating the coherent nature of the WS₂ ribbons throughout the entire array (Fig. 2, F and G). This result was reproducible, with a polarity coherence consistency ratio exceeding 99% based on the analysis of 283 ribbons (Fig. 2H and fig. S6).
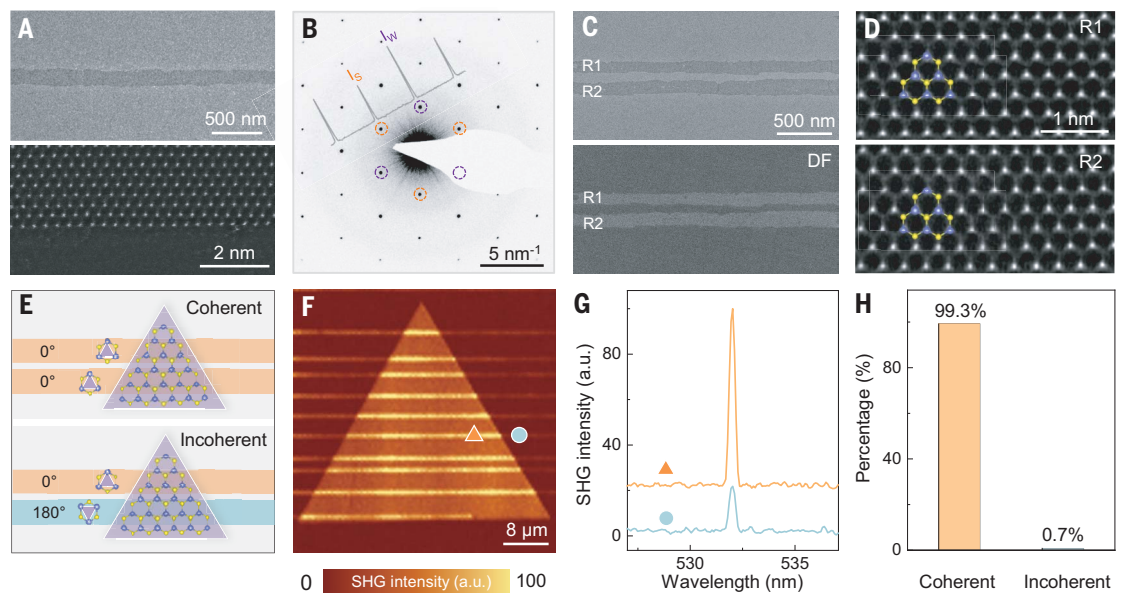
Atomic manufacturing of chirality-defined ribbons

WS₂ ribbon arrays also display consistent chirality along the axial direction. Chirality-defined

Fig. 2. Coherent polarity of the WS₂ ribbon arrays. (**A**) Low-magnification TEM image of the prepared WS₂ ribbon (upper panel) and the atomic-resolved HAADF-STEM image at the ribbon edge (lower panel). (**B**) SAED pattern of the WS₂ ribbon. The gray line is the intensity profile along the corresponding diffraction spots. The dashed violet and orange circles indicate the diffraction spots toward the W-sublattice and S-sublattice, respectively. (**C**) Uniform bright field (upper panel) and dark field (lower panel) images of two adjacent ribbons, denoted as R1 and R2, respectively.

(**D**) Corresponding atomic-resolved images of R1 (upper panel) and R2 (lower panel). (**E**) Schematic for distinguishing the polarity direction of ribbon arrays by covering a triangular WS₂ domain. (**F**) SHG mapping of the ribbons/WS₂ stacked structure. (**G**) The corresponding SHG spectra at the overlapping position [marked by the orange triangle in (F)] and the bare ribbon position [marked by the light blue circle in (F)]. (**H**) Statistical polarity coherence of the as-prepared WS₂ ribbon arrays.

Fig. 3. Axial chirality control of the WS₂ ribbons. (**A** to **D**) Epitaxial relationship illustrations (A_1 to A_3), AFM images (B_1 to B_3), optical images (C_1 to C_3), and polarization-dependent SHG patterns (D_1 to D_3) of representative zigzag (ZZ-R), armchair (AC-R), and chiral (C-R) ribbons, respectively. The pink, white, and blue balls in (A_1 to A_3) represent the top O atoms, bottom O atoms, and Al atoms, respectively. The upper panels in B_1 to B_3 are low-magnification images and the lower panels are corresponding atomic-resolved AFM images. The measurements in D_1 to D_3 are the parallel component of the total SHG intensities.
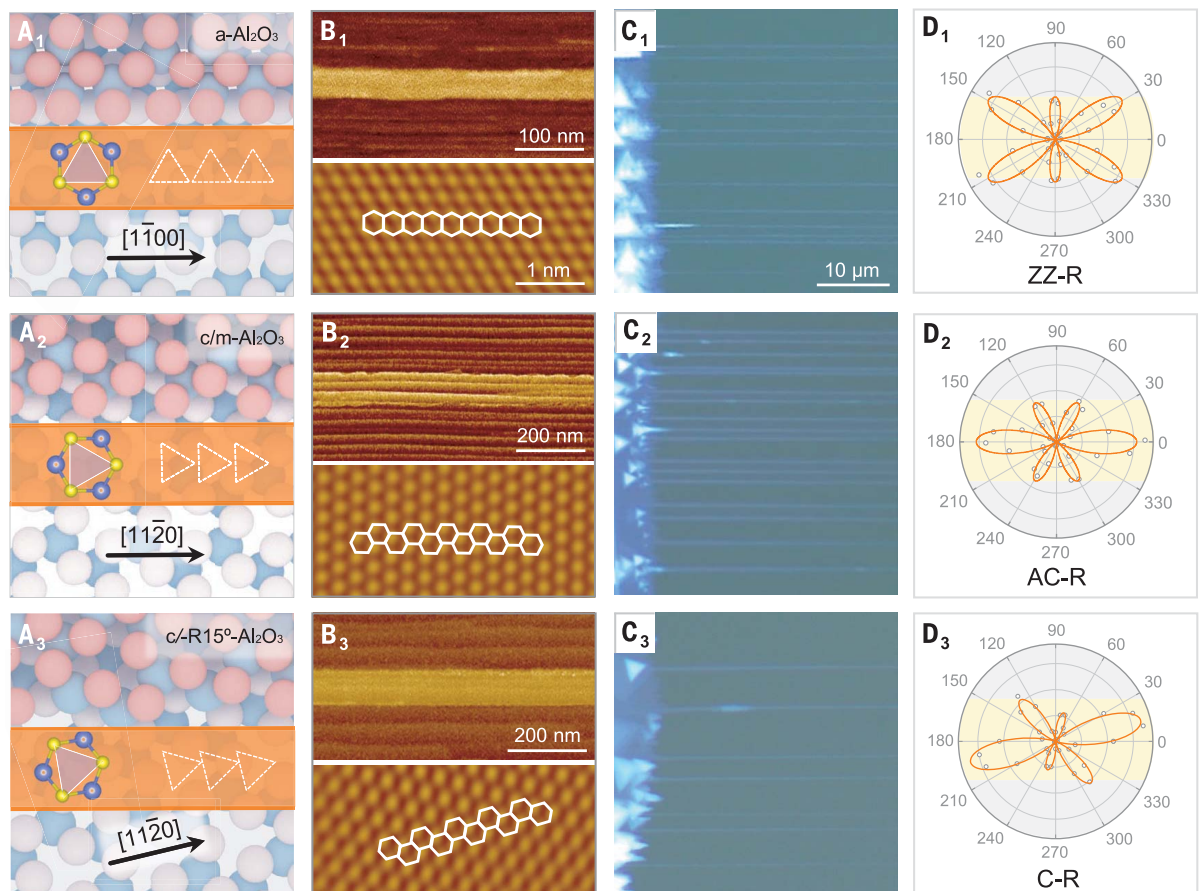
growth of TMD ribbons relies on atomic-scale precise manufacturing. In the case of the ZZ-Rs, the axis orientation is consistently guided along the crystallographic direction of $[1\bar{1}00]$ on the a-Al_2O_3 (fig. S7). This alignment has been well documented for guiding the orientation of carbon nanotube or nanowire arrays benefiting from the high-density atomic steps (31, 32). Moreover, the zigzag chains ($< 11\bar{2}0 >$ direction of WS_2) are unidirectionally arranged along the $[1\bar{1}00]$ direction of a-Al_2O_3 as a result of the couplings between TMD and the a-Al_2O_3 lattice (33–35). Utilizing this manufacturing strategy, the relative angle of 0° between the WS_2 ribbon axis and zigzag chains can be fixed, and

accounts for the coherent ZZ-R arrays (Fig. $3A_1$). Atomic force microscopy (AFM) images demonstrate the ribbon epitaxy along the restricted orientation of $[1\bar{1}00]$ (Fig. $3B_1$, top panel) with a well-determined zigzag chain arrangement (Fig. $3B_1$, bottom panel). This feature can be visualized by an optical microscope in which the edges of intensively nucleated WS_2 triangular domains are parallel to the ribbon axis (Fig. $3C_1$ and fig. S8A). In addition, the depolarization effect of the 1D structure leads to a twofold distorted SHG pattern (Fig. $3D_1$), which is consistent with the numerical simulated results (fig. S9). The relative angle between the zigzag edge (direction of minimum

SHG intensity) and the ribbon axis is identified to be 0°, which demonstrates the successful construction of the ZZ-Rs on a-Al_2O_3.

To obtain armchair ribbons (AC-Rs), vicinal c-plane sapphire (with a miscut toward the M-axis of $< 1\bar{1}00 >$, denoted as c/m Al_2O_3) was used as a template for WS_2 lattice epitaxy. As shown in Fig. $3A_2$, armchair chains ($< 1\bar{1}00 >$ direction of WS_2) could be strongly arranged along the $[11\bar{2}0]$ direction of c-Al_2O_3 as previously reported (36, 37). In addition, the aligned steps were artificially constructed from the miscut of sapphire and effectively guided the ribbon axis in the $[11\bar{2}0]$ direction. This synergistic effect led to a 30° chiral angle;
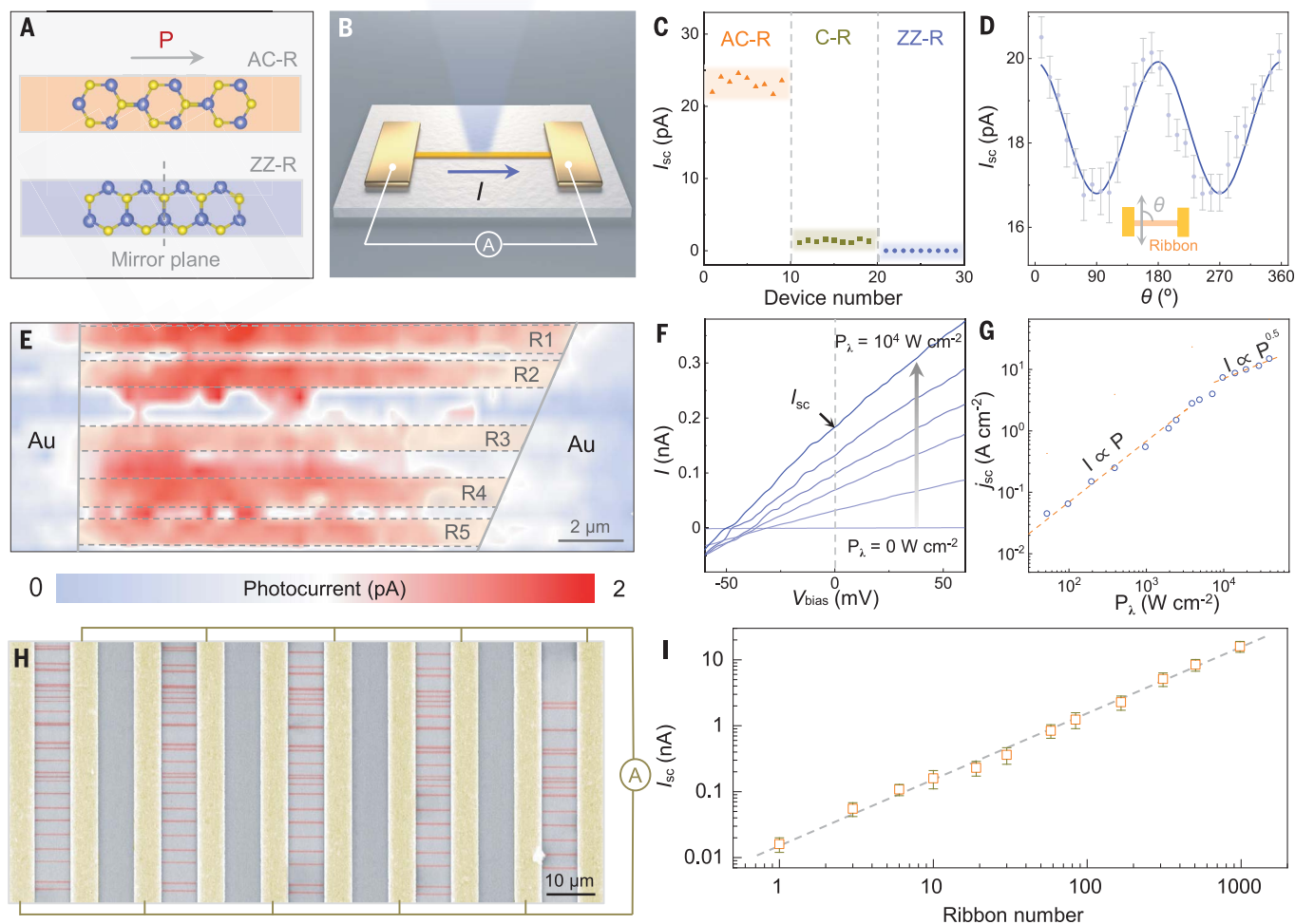

Fig. 4. Integration of chirality-dependent BPVE of WS_2 ribbons.
(**A**) Spontaneous polarization is generated in AC-Rs while it vanishes in ZZ-Rs. (**B**) Schematic of the ribbon-based BPVE device. (**C**) Short-circuit current (I_{sc}) distributions of armchair (orange triangles), chiral (dark yellow squares), and zigzag (blue circles) ribbons measured under 450 nm laser illumination with a power density of ~10^4 W cm^{-2}. (**D**) Polarization-dependent I_{sc} of AC-R with ~150-nm width. The blue line is the fitting curve of the corresponding data. Insert shows the definition of the polarization angle θ of the incident linear polarized laser. (**E**) I_{sc} spatial distribution mapping of a device comprising five coherent AC-Rs, in which the dashed outlines indicate the ribbons and the gray lines

indicate the electrode edges. (**F**) Representative *I-V* characteristics of 10-armchair ribbon assembly measured with the 450-nm laser at different illumination power densities ranging from 0 to 10^4 W cm^{-2}. (**G**) Incident power density dependence of short-circuit current density (j_{sc}) for an individual AC-R with a crossover from a linear to a square root relationship. (**H**) False-color SEM image comprising hundreds of coherent armchair ribbon channels integrated by designed interdigital electrode pairs. The WS_2 ribbons are shown in dark red and the electrodes are shown in yellow. The region of ribbons out of the channels were etched away. (**I**) Collective photocurrent evolution of an integrated ribbon array with individual numbers.

i.e., the formation of armchair ribbons (Fig. 3, B_2 to D_2, and fig. S8B). Notably, the armchair arrays still retained unidirectional polarity (fig. S10). Theoretical calculations revealed that the S-terminated zigzag edge was more affiliated with the Na_2WO_4 particle, which exhibited 3.44 eV/nm lower interfacial energy than that of the twinned configuration (fig. S11). Therefore, this ribbon-precursor interface thermodynamically dominated the unipolarity growth manner of armchair ribbons.

This manufacturing strategy enables the chirality of ribbons to be predefined by tuning the relative angles between the ribbon axis and lattice chain direction. For example, to obtain ~15° chiral ribbons (C-Rs), c-plane sapphire substrate with the miscut direction rotated clockwise by ~15° from the M-axis (denoted as c/-R15° Al_2O_3; see fig. S12) is specifically customized. The armchair chains are still arranged along the $[11\bar{2}0]$ direction of c-Al_2O_3 as that of the AC-Rs whereas the steps guiding the ribbon axis are 15°-off from the $[11\bar{2}0]$ direction (Fig. 3A₃). This design successfully produced ~15°-chiral-angle ribbons (Fig. 3, B_3 to D_3, and fig. S8C). Notably, the SHG pattern exhibits a reduced symmetry without mirror plane, with its maximum intensity direction being rotated ~15° counterclockwise from the axis, providing information about the handedness (Fig. 3D₃). Apparently, a customized c/+R15° (counterclockwise rotated ~15° from the M-axis) sapphire substrate is particularly effective for growing right-handed ~15° C-Rs (fig. S13).

In our design, the precise structure of ribbons was determined by the following aspects: (i) The couplings between WS_2 and the substrate surface determine the lattice orientation of the grown WS_2. (ii) The couplings between the Na_2MoO_4 precursor and the substrate step edges guide the unidirectional motion of seeded particles, setting the ribbon axis. (iii) The interface between WS_2 and the Na_2MoO_4 precursor prevents the twinned island formation and thermodynamically drives the unipolarity-terminated growth. It displays the versatility of our strategy in designing the polarity and chirality (including handedness) simultaneously, which has long been an extreme challenge in 1D systems.

Chirality-dependent and integratable bulk photovoltaic effect

The BPVE in 1D WS_2 ribbons displays chirality-dependent characteristics. The armchair ribbon possesses spontaneous polarization due to its broken inversion symmetry in the axial direction (Fig. 4A), resulting in the generation of a self-driven BPVE photocurrent upon light illumination. By contrast, the net polarization in the mirror symmetric zigzag ribbon is nullified, generating no spontaneous photocurrent.

We detected the BPVE photocurrent of the ribbons using a two-terminal device under a laser excitation wavelength of 450 nm (Fig. 4B). The short-circuit currents (I_{sc}) of armchair ribbons exhibit channel length–dependent BPVE, with a typical I_{sc} around 20 pA at the length of ~30 μm (Fig. 4C and fig. S14). Moreover, the chiral ribbons exhibit a weaker BPVE response (~1 pA), which arises from the tilted lattice chains from the axis whereas no responses are observed in the zigzag ones. The spontaneous photocurrent intensity of individual armchair ribbons depends on the polarization of the incident light and shows a width dependence (Fig. 4D, fig. S15). It reaches its maximum when the laser polarization is parallel to the ribbon axis (θ = 0°) and decreases to the minimum at θ = 90°, confirming the alignment of polar direction along the armchair edges.

Furthermore, the positive photocurrent distribution of a ribbon array (comprising five armchair ribbons) shows no sign change across the entire channel (Fig. 4E), benefiting from their coherent polarity orientation. This feature offers an effective approach for increasing the collective photocurrent by simply increasing the number of ribbons. As displayed in Fig. 4F, around 100 pA photocurrent is achieved in the 10-armchair-ribbon assembly. It corresponds to a short-circuit current density of 0.37 A cm^{-2}, averaged across the cross-sectional area of the entire device. Simultaneously, the short-circuit current density displays a linear dependence on the excitation power density (P < $5×10^3$ W cm^{-2}) and transitions to a square root relationship as the light intensity further increases (Fig. 4G), which is a typical feature of BPVE rather than the photovoltaic effect caused by the Schottky barrier (38). By further integrating hundreds of ribbons and gathering photocurrents through interdigital electrode design (Fig. 4H), a substantially high collective photocurrent up to 16 nA can be accessed from ~1000 ribbons (Fig. 4I). In addition, the BPVE photocurrent can also be enhanced by increasing the thickness of ribbons (fig. S16), which illustrates the potential scalability of TMD ribbons toward junction-free BPVE solar cell arrays.

Conclusions

We developed a manufacturing strategy for the controllable growth of WS_2 ribbon arrays with defined chirality and coherent polarity. The flexibility in fabricating deterministic-structured ribbon arrays enabled the systematic investigation of chirality-dependent BPVE and the realization of robust integration of photovoltaic device arrays. Our strategy provides a versatile way for on-demand tailoring and large-scale integration of 1D materials, which will facilitate advances in self-driving on-chip electronics and optoelectronics.

REFERENCES AND NOTES

1. M.-M. Yang, D. J. Kim, M. Alexe, *Science* **360**, 904–907 (2018).
2. T. Akamatsu et al., *Science* **372**, 68–72 (2021).
3. J. Jiang et al., *Nat. Nanotechnol.* **16**, 894–901 (2021).
4. D. Yang et al., *Nat. Photonics* **16**, 469–474 (2022).
5. Y. Dong et al., *Nat. Nanotechnol.* **18**, 36–41 (2023).
6. S. Y. Yang et al., *Nat. Nanotechnol.* **5**, 143–147 (2010).
7. J. E. Spanier et al., *Nat. Photonics* **10**, 611–616 (2016).
8. M. Nakamura et al., *Nat. Commun.* **8**, 281 (2017).
9. L. Du et al., *Nat. Rev. Phys.* **3**, 193–206 (2021).
10. Y. J. Zhang et al., *Nature* **570**, 349–353 (2019).
11. M.-M. Yang, M. Alexe, *Nature* **570**, 310–311 (2019).
12. S. Li et al., *Nat. Mater.* **17**, 535–542 (2018).
13. A. Aljarb et al., *Nat. Mater.* **19**, 1300–1306 (2020).
14. Y. Deng et al., *Mater. Today* **58**, 8–17 (2022).
15. P. Yang et al., *Nat. Commun.* **13**, 3238 (2022).
16. X. Liu et al., *Nat. Commun.* **4**, 1776 (2013).
17. Z. Liu et al., *Nat. Commun.* **2**, 213 (2011).
18. Y. Chen et al., *Nat. Commun.* **8**, 15135 (2017).
19. F. Cheng et al., *Nano Lett.* **17**, 1116–1120 (2017).
20. T. Chowdhury et al., *Nat. Nanotechnol.* **15**, 29–34 (2020).
21. R. Xiang et al., *Science* **367**, 537–542 (2020).
22. X. Li et al., *Sci Adv* **7**, eabk1892 (2021).
23. Q. An et al., *Nat. Mater.* **23**, 347–355 (2024).
24. J. R. Sanchez-Valencia et al., *Nature* **512**, 61–64 (2014).
25. R. M. Jacobberger et al., *Nat. Commun.* **6**, 8006 (2015).
26. S. Zhang et al., *Nature* **543**, 234–238 (2017).
27. H. S. Wang et al., *Nat. Mater.* **20**, 202–207 (2021).
28. J. Cai et al., *Nature* **466**, 470–473 (2010).
29. Y. Zuo et al., *Nat. Commun.* **13**, 1007 (2022).
30. P. Deb et al., *Ultramicroscopy* **215**, 113019 (2020).
31. S. Han, X. Liu, C. Zhou, *J. Am. Chem. Soc.* **127**, 5294–5295 (2005).
32. D. Tsivion, M. Schvartzman, R. Popovitz-Biro, P. von Huth, E. Joselevich, *Science* **333**, 1003–1007 (2011).
33. Z. Ma et al., *Small* **16**, e2000596 (2020).
34. J. Wang et al., *Nat. Nanotechnol.* **17**, 33–38 (2022).
35. P. Zheng et al., *Nat. Commun.* **14**, 592 (2023).
36. T. Li et al., *Nat. Nanotechnol.* **16**, 1201–1207 (2021).
37. J.-H. Fu et al., *Nat. Nanotechnol.* **18**, 1289–1294 (2023).
38. Z. Liang et al., *Nat. Commun.* **14**, 4230 (2023).

SUPPLEMENTARY MATERIALS

science.org/doi/10.1126/science.adn9476
Materials and Methods
Figs. S1 to S16